Volume 16
Number 5
7 February 2024
Pages 2063-2674

Nanoscale

rsc.li/nanoscale

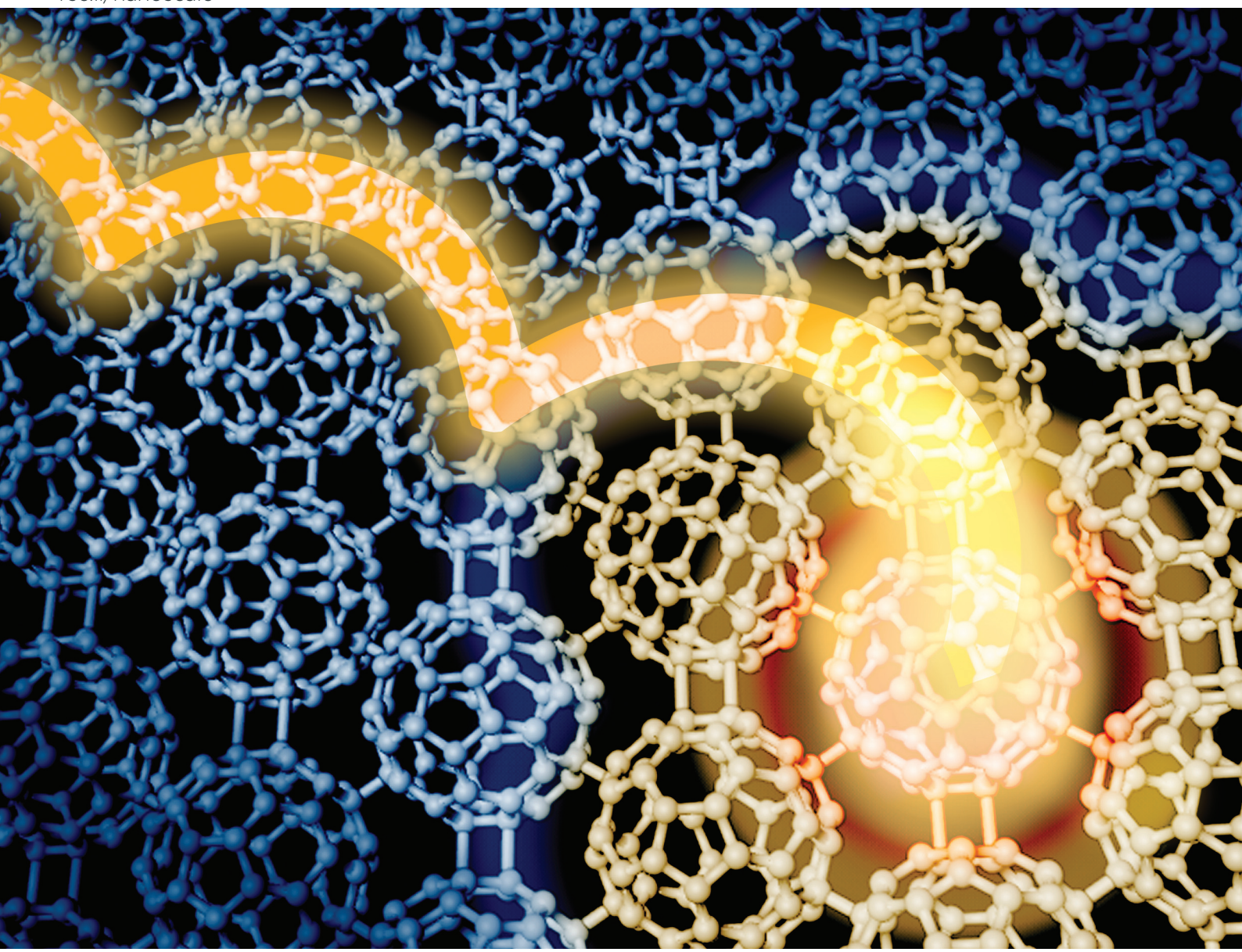

ISSN 2040-3372

ROYAL SOCIETY OF CHEMISTRY

PAPER
L. A. Ribeiro, Junior *et al.*
Large polarons in two-dimensional fullerene networks: the crucial role of anisotropy in charge transport

NCNST

Nanoscale

PAPER

Cite this: *Nanoscale*, 2024, **16**, 2337

Large polarons in two-dimensional fullerene networks: the crucial role of anisotropy in charge transport†

T. S. A. Cassiano, [a] M. L. Pereira, Junior, [b] G. M. e Silva,[a] P. H. de Oliveira Neto [a] and L. A. Ribeiro, Junior *[a,c]

The recent synthesis of a two-dimensional quasi-hexagonal-phase monolayer network of C_{60} molecules, known as $qHPC_{60}$, holds significant promise for future semiconductor applications. However, the mechanism behind charge transport in these networks remains unknown. In this study, we developed a Holstein–Peierls Hamiltonian model to investigate charge transport in $qHPC_{60}$, incorporating both local and non-local electron–phonon couplings. Our computational approach involved identifying suitable semi-empirical parameters to realize the formation of stable polarons in this material. The results unveiled the formation of stable large polarons as the primary carriers in the charge transport throughout $qHPC_{60}$. To explore polaron transport properties, we conducted dynamic simulations within the picosecond time scale while subjecting the system to an external electric field. Our analysis emphasized the substantial influence of anisotropy on shaping mobile polarons, with an anisotropy coefficient of at least 50%. The polarons exhibited velocities within the acoustic regime ranging from 0.5–1.5 nm ps^{-1}. While these velocities are comparable to those observed in high-end organic molecular crystals, they are considerably lower than those in graphene and conducting polymers. With $qHPC_{60}$ possessing a semiconducting band gap of approximately 1.6 eV, our findings shed light on its potential application in flat electronics, overcoming the null-gap predicament of graphene.

Received 28th September 2023,
Accepted 5th December 2023

DOI: 10.1039/d3nr04920e

rsc.li/nanoscale

1. Introduction

Organic molecular crystals (OMCs) offer a promising alternative for the future of optoelectronics.[1,2] OMCs are composed of molecular units arranged in a way that balances various intermolecular interactions, including van der Waals, multipole, and π-stacking.[3] There is a plethora of different OMCs types[4] behind the development in novel photovoltaics,[3] field-effect transistors,[5–7] thermal sensing,[8,9] and flexible nanoelectronic devices.[10–12] A crucial aspect that greatly influences the efficiency of these applications is the mechanism of charge transport, which requires a comprehensive understanding.[2]

The attributes of OMCs are predominantly determined by the properties of the molecular units and their arrangement within the lattice.[4] In this regard, the C_{60} fullerene is a strong candidate for potentially superior molecular crystal systems.[13] For instance, its high electron affinity and mechanical robustness make it highly suitable as an electron acceptor in photovoltaic applications.[4,14–18] Notably, previous investigations have highlighted the promising potential of C_{60}-based crystals for applications such as nanocages, nanolubricants, and optoelectronics, thanks to their strain-tunable semiconducting characteristics.[19]

Recently, a groundbreaking experimental achievement[20] has led to the realization of a two-dimensional quasi-hexagonal-phase monolayer network of C_{60} molecules, referred to as $qHPC_{60}$. In this remarkable material, the molecules are interconnected through strong covalent bridge bonds, resulting in a well-defined and distinct topological structure. $qHPC_{60}$ exhibits excellent thermodynamic and mechanical stability,[21,22] along with a desirable band gap of 1.6 eV for potential semiconducting applications.[23,24] Furthermore, it showcases remarkable in-plane anisotropic properties.[20,25,26]

These exceptional characteristics have already ignited advancements in the fields of thermoelectric applications[27]

[a]*University of Brasília, Institute of Physics, 70.910-900, Brasília, Brazil. E-mail: ribeirojr@unb.br*
[b]*International Center of Physics, Institute of Physics, University of Brasília, Faculty of Technology, Department of Electrical Engineering, 70910-900, Brasília, Brazil*
[c]*Computational Materials Laboratory, LCCMat, Institute of Physics, University of Brasília, 70910-900, Brasília, Brazil*

† Electronic supplementary information (ESI) available. See DOI: https://doi.org/10.1039/d3nr04920e

and photocatalysis.[28] Despite these significant developments, the topic of charge transport in this material has yet to be studied. To the best of our knowledge, no reports have investigated the stationary and dynamic properties of carriers or their underlying mechanisms. Therefore, conducting a comprehensive investigation of charge transport in fullerene networks becomes crucial, serving as the primary objective of the present study.

An effective description of charge transport is crucial for the optimal performance of optoelectronic devices.[2,4] This process is imperative to thoroughly understand and characterize new materials before incorporating them into practical applications. In the case of OMCs, the first step involves investigating the properties of the charge carriers, which are manifested as polarons. These collective excitations are self-trapped and half-spin structures of charge e, which emerge from the energy balance resulting from the excess charge.[29] To provide a comprehensive theoretical framework, non-adiabatic Hamiltonian models[4,30,31] are the most suitable choice as they treat electronic and lattice phenomena simultaneously.

In OMCs, various modeling approaches have been employed to explore the charge transport mechanism, aiming to reproduce experimentally observed phenomena such as the temperature dependence of mobility in ultrapure crystals.[32,33] However, the current state of some of these approaches provides limited insight into the behavior of charge transport in networks. An appropriate model must explicitly consider the interplay between intra- and intermolecular interactions, considering the effects of anisotropy.[34–40] This requirement comes from the fact that both experimental and theoretical works indicate that qHPC$_{60}$ possesses high average intramolecular phonon frequencies[37,41] and strong intermolecular covalent bonds.[20,21]

Herein, we conducted a comprehensive investigation into the charge transport properties of qHPC$_{60}$. To accomplish this, we employed a non-adiabatic model Hamiltonian based on the Holstein–Peierls approach.[42] Our computational protocol takes into consideration the coupling between intra- and intermolecular interactions, as well as the anisotropy of the system. The primary focus of our investigation was to examine the stationary properties of qHPC$_{60}$ and identify the specific conditions under which mobile carriers can emerge in the material. Furthermore, we performed dynamic simulations to characterize the velocity regime of the quasiparticles in this system.

2 Methodology

2.1 Model Hamiltonian

In our modeling of qHPC$_{60}$, the C$_{60}$ molecules are considered as individual sites within a molecular matrix. For simplification purposes, the hexagonal lattice is approximated to a square shape, as depicted in Fig. 1(a). In this representation, the position of each site is determined by the line index (in the x-direction) and the column index (in the y-direction) on a square grid molecular matrix. For example, the fullerene site shown at the center of this figure is located at position (i,j), while its rightmost neighbor is at position $(i+1,j)$.

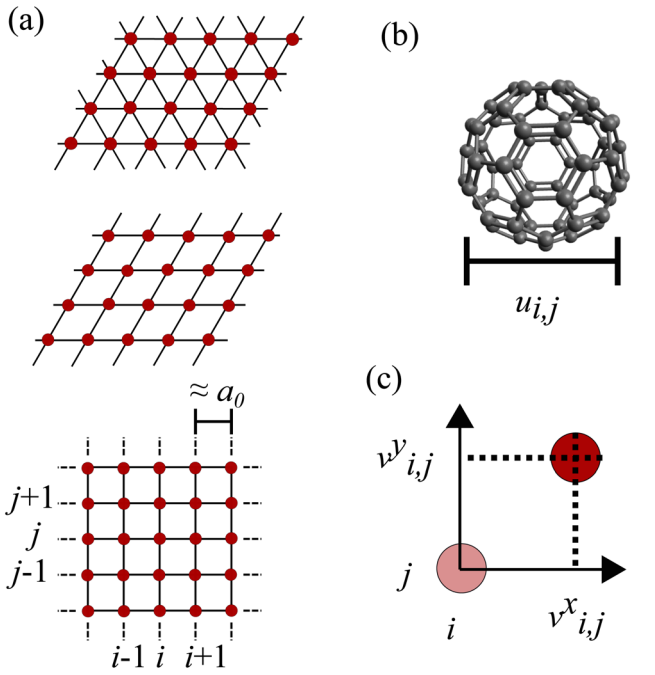

Fig. 1 A schematic representation of qHPC$_{60}$ is depicted. In (a), the molecular matrix of the system is shown, where each red disk represents a fullerene molecule connected to four neighboring molecules. The hexagonal lattice is approximated to a square shape. Panel (b) illustrates the internal lattice deformation order parameter $u_{i,j}$ at a specific site (i,j). (c) represents the lattice displacements of the molecule (i,j) in the x ($v^x_{i,j}$) and y ($v^y_{i,j}$) directions.

The Hamiltonian comprises two terms: the intramolecular term H_{intra} and the intermolecular term H_{inter}. Each term encompasses both electronic and lattice components:[36,40,43,44]

$$\begin{aligned} H_{\text{intra}} &= H^{\text{elec}}_{\text{intra}} + H^{\text{latt}}_{\text{intra}}, \\ H_{\text{inter}} &= H^{\text{elec}}_{\text{inter}} + H^{\text{latt}}_{\text{inter}}. \end{aligned} \tag{1}$$

The explicit form of the electronic contribution for the intramolecular part, $H^{\text{elec}}_{\text{intra}}$, in second quantization formalism, is

$$H^{\text{elec}}_{\text{intra}} = \sum_{i,j} \alpha_{\text{intra}} u_{i,j} \left(C^{\dagger}_{i,j} C_{i,j} \right). \tag{2}$$

In this equation, $u_{i,j}$ is the intramolecular lattice distortion of the molecule located at position (i,j) (see Fig. 1(b)). The operator $C^{\dagger}_{i,j}$ creates an electron in the lowest unoccupied molecular orbital (LUMO) of the (i,j)-th molecule, while $C_{i,j}$ removes an electron from the same orbital. The interaction between the electron and the lattice, encompassing both lattice and electronic effects, is governed by the intramolecular (or local) electron–phonon coupling constant α_{intra}.

In contrast, the intramolecular lattice interaction $H^{\text{latt}}_{\text{intra}}$ is treated within the framework of the harmonic approximation.

In this approximation, the intramolecular lattice deformation of each molecule is modeled as a harmonic oscillator with a mass M_{intra} and a spring constant K_{intra}, described by the following expression:

$$H_{\text{intra}}^{\text{latt}} = \frac{M_{\text{intra}}}{2}\sum_{i,j}\dot{u}_{i,j}{}^2 + \frac{K_{\text{intra}}}{2}\sum_{i,j}u_{i,j}{}^2. \tag{3}$$

The electronic term $H_{\text{inter}}^{\text{elec}}$ follows the tight-binding approach

$$\begin{aligned} H_{\text{inter}}^{\text{elec}} = &\sum_{i,j}\left(J_{i+1,j}^{x}C_{i+1,j}^{\dagger}C_{i,j} + h.c.\right) \\ &+ \sum_{i,j}\left(J_{i,j+1}^{y}C_{i,j+1}^{\dagger}C_{i,j} + h.c.\right), \end{aligned} \tag{4}$$

where $J_{i+1,j}^{x}$ is the hopping integral linking the horizontally aligned first neighbor molecules (i,j) and $(i+1,j)$, while $J_{i,j+1}^{y}$ connects the molecules (i,j) and $(i,j+1)$.

When constructing the network model, we take into account the spatial variation of the hopping integrals, which arises from the inherent flexibility of the material. To capture this effect, we employ a first-order expansion around the unperturbed hopping terms J_0^x and J_0^y. Additionally, the interaction can be adjusted to incorporate the influence of an external electric field using the Peierls substitution.[45–47]

In this context, we find it advantageous to select the potential vector aligned with the x-direction as $A_x(t) = -cE_{x0}t$, where E_{x0} is the strength of the electric field. By combining these two adjustments, we arrive at the following expression for the transfer integrals:[36,44]

$$\begin{aligned} J_{i+1,j}^{x} &= \left(J_0^x - \alpha_{\text{inter}}\left(v_{i+1,j}^{x} - v_{i,j}^{x}\right)\right)e^{i\gamma A_x(t)}, \\ J_{i,j+1}^{y} &= \left(J_0^y - \alpha_{\text{inter}}\left(v_{i,j+1}^{y} - v_{i,j}^{y}\right)\right). \end{aligned} \tag{5}$$

Here, $\gamma \equiv ea_0/\hbar c$, in which a_0 is the lattice parameter and c is the speed of light. α_{inter} is the intermolecular (or non-local) electron–phonon coupling constant, while $v_{i,j}^{x}$ and $v_{i,j}^{y}$ are, respectively, the relative longitudinal and transversal lattice displacements of the molecule (i,j) away from its pristine configuration.

Fig. 1(c) illustrates the meaning of these two quantities. The light red disk corresponds to the site (i,j) within a uniformly spaced grid arrangement. By considering this position as the origin of the coordinate system, the molecule's placement can be altered by $v_{i,j}^{x}$ and $v_{i,j}^{y}$ along the x and y axes, respectively, due to bond distortions. As a result, the site assumes a new optimized configuration, as depicted by the solid red disk. For future reference, we define the anisotropy coefficient as $1 - J^y0/J^x0$ with the assumption that $J^y0 \leq J^x0$. Consequently, the coefficient reflects the disparity between the two hopping integrals, with a larger coefficient indicating a greater difference.

The intermolecular lattice term is treated using the same approximation as the intramolecular case. We assume that each molecular site, with a mass of M_{inter}, is connected to its four first neighbors through harmonic oscillators characterized by a spring constant of K_{inter}. In simpler terms,

$$\begin{aligned} H_{\text{inter}}^{\text{latt}} = &\frac{K_{\text{inter}}}{2}\sum_{i,j}(\Delta x_{i,j})^2 + \frac{K_{\text{inter}}}{2}\sum_{i,j}(\Delta y_{i,j})^2 \\ &+ \frac{M_{\text{inter}}}{2}\sum_{i,j}(\dot{v}_{i,j}{}^x)^2 + \frac{M_{\text{inter}}}{2}\sum_{i,j}(\dot{v}_{i,j}{}^y)^2. \end{aligned} \tag{6}$$

The quantities $\Delta x_{i,j} = v_{i+1,j}^{x} - v_{i,j}^{x}$ and $\Delta y_{i,j} = v_{i,j+1}^{y} - v_{i,j}^{y}$ represent the distortions in bond lengths for the horizontal and vertical links connecting the neighboring sites, respectively.

The backpropagation (RPROP) algorithm is used to obtain the stationary solution of the molecular arrangement.[48] This algorithm returns a set of eigenvectors $|\psi_k(t)\rangle$ corresponding to the electronic Hamiltonian $H^{\text{elec}} = H_{\text{intra}}^{\text{elec}} + H_{\text{inter}}^{\text{elec}}$, as well as the optimized lattice configuration represented by the sets $u_{i,j}$ and $v_{i,j}^{x/y}$. These optimizations are performed without any time-dependent external influences.[49] The eigenvector with the lowest energy, denoted as $|\psi(t_0)\rangle$, represents the stationary polaron state and is the initial state for the subsequent dynamics.

Time evolution is made by simultaneously evolving the electronic and lattice degrees of freedom. The former is given by the time-dependent Schödinger equation that, for a time increment $\mathrm{d}t$, can be expressed as follows:

$$|\psi(t+\mathrm{d}t)\rangle = e^{-iH^{\text{elec}}(t)\mathrm{d}t/\hbar}|\psi(t)\rangle. \tag{7}$$

Expanding the right side over the basis of the instantaneous electronic Hamiltonian eigenstates $|\varphi_l(t)\rangle$ leads to

$$|\psi(t+\mathrm{d}t)\rangle = \sum_{l} e^{-i\varepsilon_l(t)\mathrm{d}t/\hbar}\langle\phi_l(t)|\psi(t)|\phi_l(t)\rangle, \tag{8}$$

where $\{\varepsilon_l(t)\}$ are the corresponding eigenvalues. By projecting both sides to the molecular matrix position vector $|i,j\rangle$, we reach the explicit form for the time evolution of the wave function

$$\begin{aligned} \langle i,j|\psi(t+\mathrm{d}t)\rangle \equiv \psi(i,j,t+\mathrm{d}t) = \sum_{l}\Bigg(&e^{-i\varepsilon_l(t)\mathrm{d}t/\hbar} \\ &\times\left[\sum_{m,n}\phi_l(m,n,t)\psi(m,n,t)\right]\phi_l(i,j,t)\Bigg). \end{aligned} \tag{9}$$

The lattice evolution is determined by solving the Euler–Lagrange equations for the expected value of the Lagrangian using Ehrenfest dynamics. The equation governing the intramolecular motion is given by:[36,50]

$$M_{\text{intra}}\ddot{u}_{i,j}(t) = -K_{\text{intra}}u_{i,j}(t) - \alpha_{\text{intra}}\rho_{i,j;i,j}, \tag{10}$$

while the intermolecular are

$$\begin{aligned} M_{\text{inter}}\ddot{v}_{i,j}^{x}(t) = &-K_{\text{inter}}\left(2v_{i,j}^{x}(t) - v_{i+1,j}^{x}(t) - v_{i-1,j}^{x}(t)\right) + \\ &-\alpha_{\text{inter}}\left([\rho_{i,j,i-1,j}(t) - \rho_{i+1,j,i,j}(t)]e^{-i\gamma A_x(t)} + c.c.\right) \end{aligned} \tag{11}$$

and

$$\begin{aligned} M_{\text{inter}}\ddot{v}_{i,j}^{y}(t) = &-K_{\text{inter}}\left(2v_{i,j}^{x}(t) - v_{i,j+1}^{x}(t) - v_{i,j+1}^{x}(t)\right) + \\ &-\alpha_{\text{inter}}(\rho_{i,j,i,j-1}(t) - \rho_{i,j+1,i,j}(t) + c.c.). \end{aligned} \tag{12}$$

Here, $\rho_{i,j,m,n}(t) \equiv \psi(i,j,t)\psi(m,n,t)^*$ is the element (i,j,m,n) of the molecular electronic density matrix. Then, the equations of motion can be numerically integrated using the instantaneous velocities and accelerations within the scope of the velocity-Verlet algorithm. As a result, one obtains the updated lattice coordinates.

We highlight that the electronic Hamiltonian changes as the lattice evolves. Therefore, succeeding each time step dt, H^{elec} must be re-diagonalized to obtain a new set φ_l to update the electronic states *via* eqn (9).[36]

The intramolecular parameters of the hybrid (electronic + nuclear) Hamiltonian used in this study are as follows: α_{intra} = 0.3 eV Å^{-1},[37] K_{intra} = 16.51 eV Å^{-2},[37] $M_{\text{intra}} = 7.5 \times 10^{10}$ eV(as/Å), K_{inter} = 1.26 eV Å^{-2},[21] and $M_{\text{inter}} = 1.5 \times 10^{11}$ eV(as/Å). The lattice parameter a_0, representing the center-to-center distance between neighboring fullerenes, is 8.6 Å. This value is obtained by summing the diameter of a molecule (approximately 7 Å (ref. 51 and 52)) with the bridge bond length of 1.64 Å.[21] An external electric field of E_{0x} = 2 mV Å^{-1} is applied. The remaining parameters will be discussed in detail in the Results section.

2.2 IPR and polaron formation energy

The Holstein–Peierls model Hamiltonian exhibits two distinct types of polaron solutions: the Holstein (small) polaron and the Peierls (large) polaron.[37] The Holstein polaron arises when the lattice interactions are sufficiently strong to confine the entire charge within a single molecular site. In contrast, the Peierls polaron occurs when there is a more balanced energy distribution between the electronic and lattice components, resulting in self-trapped structures that extend over multiple molecular units.

In addition to visually confirming the charge accumulation profile, the inverse participation ratio (IPR) serves as a distinguishing metric for the two types of carriers. The IPR is a dimensionless coefficient that quantifies the cohesion of the quasiparticle throughout the network. Its explicit form is given by:

$$\text{IPR} = \frac{\sum_{i,j} \left|\rho_{i,j}\right|^2}{\left(\sum_{i,j} \left|\rho_{i,j}\right|^2\right)}, \tag{13}$$

where $\rho_{i,j} \equiv \rho_{i,j;i,j} = |\psi_k(i,j,t)|^2$.

Solutions with an IPR ranging from 0.0 to 0.4 represent free carriers that are not bound to phonon clouds, lacking the intrinsic coupled nature of a quasiparticle. On the other hand, Peierls polarons emerge when the IPR falls within the range of 0.4 to 0.75, while higher values (up to IPR = 1.0) correspond to Holstein carriers. In the following analysis, we will employ the IPR to explore the parameter space and identify stable polaron configurations. By examining their collective response, we can estimate the intermolecular transport behavior within the network.

Another attribute of interest is the polaron formation energy (E_{p}), an indicator of carrier stability and physical realism of the modeling,[42,43]

$$E_{\text{p}} = 2(J_0^x + J_0^y) - E^{+/-}. \tag{14}$$

Here, $E^{+/-}$ denotes the total energy of the lattice when hosting a positive/negative polaron. Solutions with $E_{\text{p}} > 0$ eV are considered stable, irrespective of their magnitude. However, carriers exhibiting excessively high E_{p} values (at least, greater than 2 eV) indicate an inappropriate parameter set for describing charge transport in the material. To obtain a realistic depiction of intermolecular charge transport, we will rely on E_{p} and IPR to identify configurations with stable polaron solutions.

Reducing the hexagonal molecular network of qHPC$_{60}$ to a square lattice means neglecting sites from one of the hexagonal diagonals. This simplification is reasonable and convenient since it disregards only molecules outside the transport line.[37] If the external electric field is aligned with the bond direction, the resulting charge transport mechanism should be a good representation of the materials' properties.

3. Results

We begin the study by finding the suitable range of $J_0^{x/y}$ and α_{inter} to simulate qHPC$_{60}$. This can be done by examining the stationary polaron properties. In other words, the carrier formation in the absence of an external electric field. A comprehensive discussion regarding this investigation is presented in the ESI.† First, a preliminary scan indicated that stable polarons emerge when $\alpha_{\text{inter}} \approx 0.2\text{–}0.3\alpha_{\text{intra}}$. Furthermore, as evidenced by Fig. S1,† a direct comparison of IPR and E_{p} for diverse combinations of $J_0^{x/y}$ determines a range of suitable values of hopping integrals. It is found that qHPC$_{60}$ is best represented when J_0^x is within the range 200–250 meV and J_0^y is restricted to be between 50 and 100 meV. Finally, Fig. S2† exposes the effects of anisotropy on the polaron morphology. The results suggest that anisotropy is essential for an accurate physical description of the model qHPC$_{60}$. Without it, the charge carriers would exhibit nonphysical high effective masses. With this finding in mind, an important question arises: what is the optimal degree of anisotropy to adequately describe the charge transport mechanism in qHPC$_{60}$? To answer this question, we proceed to assess the dynamic stability of the carriers.

Fig. 2 depicts the heatmap illustrating the dynamical stability of polarons under the influence of an external field of E_{0x} = 2 mV Å^{-1}. In this figure, red configurations indicate immobile carriers, while blue configurations represent mobile ones. It also reveals that isotropy has a detrimental effect on dynamical stability, despite the confirmed stationary cohesion observed in Fig. S1.† When J_0^y exceeds $0.5J_0^x$ within the range of [200–250] meV for J_0^x, the resulting polarons are consistently immobile. This finding aligns with our earlier qualitative analysis of the impact of anisotropy on polaron morphology, as

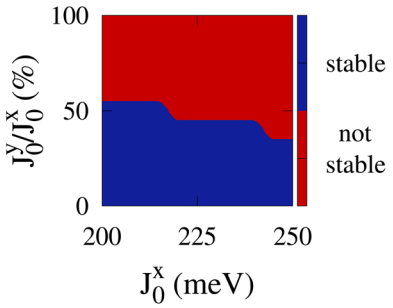

Fig. 2 The dynamical stability of polaron carries over diverse anisotropy and hopping regimes. Configurations in red are not stable. On the other hand, the blue ones are.

demonstrated in Fig. S2,† where isotropy was associated with heavier carriers.

Interestingly, instability can persist even after the polaron surpasses the energy barrier that initially trapped it. In certain simulated scenarios (not depicted here), although the structure initiates movement, the stored energy is so substantial that the quasiparticle rapidly loses its coherence and transitions into a delocalized band state, resulting in destabilization. Another noteworthy observation is that achieving stability becomes increasingly challenging as the value of J_0^x grows, which aligns with previous investigations conducted on other OMCs.[37,50]

The identification of dynamically stable carriers strongly supports the existence of polaron-mediated transport in the model qHPC$_{60}$. However, the intrinsic transport properties of the quasiparticle still need to be uncovered. To address this objective, we will investigate charge transport while confining the analysis to isotropy levels within the range of [0–50]%.

We now investigate the polaron dynamical properties in a model qHPC$_{60}$ for a fixed value of J_0^x = 200 meV. The qualitative picture presented here extends to the other configurations. Fig. 3(a) and (b) display, respectively, the position and average velocity of the carriers as a function of time for isotropy levels of 0 (blue), 20 (red), and 50% (green).

All carriers exhibit similar dynamics in a qualitative sense. As time progresses, the polaron gradually acquires momentum from the electric field, resulting in minimal variation in its initial position until 0.3 ps. Subsequently, when the polaron accumulates sufficient energy to surpass the potential barrier imposed by the lattice, typically around 0.5 ps, it undergoes pronounced drift, traversing multiple molecular units until the simulation concludes. Throughout this latter stage of polaron transport, the position of the polaron demonstrates nearly linear changes over time, leading to a tendency of constant velocity.

The distance traveled by the polaron depends on the ratio of J_0^y/J_0^x. During the 0.0–1.2 ps interval, the carriers reach their maximum velocity, representing the mobilization phase characterized by the time required for the polaron to achieve a constant velocity. Subsequently, the polaron releases phonon breathers, a mechanism discussed in detail later, to dynamically stabilize its motion, reaching a terminal velocity regime. This behavior is also found in numerous highly confined materials[45–47,53–56] and intermolecular arrangements,[36,37,50] with a strong electronic and lattice interplay.

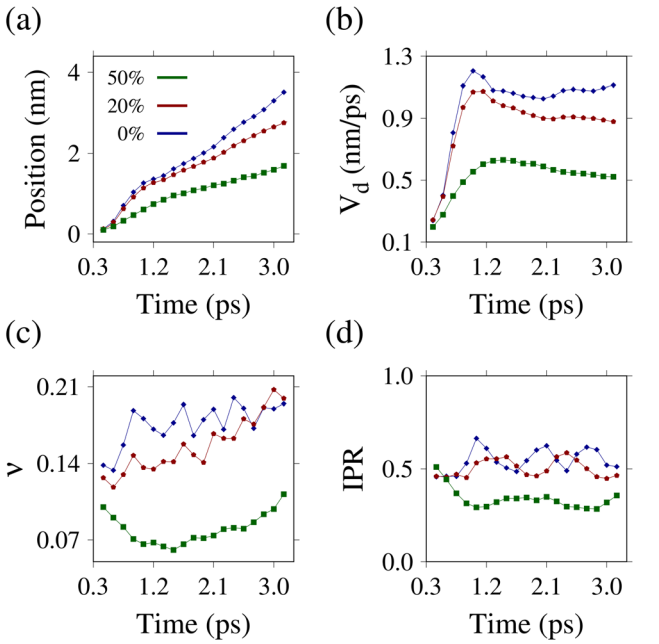

Fig. 3 Time evolution of (a) polaron position, (b) its related mean velocity, (c) $\nu = H_{intra}/H_{inter}$, (d) and mean IPR. The colors label the levels of anisotropy: green (50%), red (20%), and blue (0%).

Since Fig. S2† showed a significant change on the polaron morphology due to the electronic anisotropy, one can anticipate that higher levels of anisotropy lead to faster carriers. For example, when $J_0^y = 0.5J_0^x$, the polaron travels a distance of 2 nm within 3 ps. In contrast, the polaron in the fully anisotropic configuration ($J_0^y = 0$) covers a distance of 3.3 nm over the same time period. This behavior is illustrated in the velocity curves depicted in Fig. 3(b). At 3 ps, the velocities of the carriers increase with the degree of anisotropy: (50%) 0.5 nm ps^{-1}, (20%) 0.9 nm ps^{-1}, and (0%) 1.2 nm ps^{-1}. These findings align with our previous observations on the polaron localization, as isotropy leads to an increase in the polaron's effective mass. Conversely, when J_0^x is significantly greater than J_0^y, the energy barrier associated with motion along the specific molecular line where the polaron charge is concentrated diminishes. This process reduces the polaron's effective mass, enabling faster drift.

Now we discuss other underlying dynamical properties for the polaron to gain more insights into its transport mechanism on model qHPC$_{60}$. Fig. 3(c) illustrates the variation of the ratio between the calculated intramolecular and intermolecular energies, denoted as $\nu = H_{intra}/H_{inter}$, over time. A higher value of ν indicates a greater contribution of intramolecular interactions to the total energy. In general, the curves exhibit minor fluctuations around a mean value. In the one-dimensional limit ($J_0^y = 0$), ν is significantly higher compared to the case when $J_0^y = 0.5J_0^x$. This discrepancy arises from

the fact that the intermolecular electronic energy (eqn (4)) becomes negligible when J_0^y is zero. Consequently, the ratio ν is naturally higher in this scenario compared to cases where there is any hopping contribution in the y-direction.

The dynamical evolution of IPR displays a similar setting, as shown in Fig. 3(d). As time advances, the IPR values oscillate around a medium value of about 0.5 for 20% and 0% and around 0.4 for 50% of anisotropy. The fluctuation results from the transport mechanism of large polarons that consists of a cycle of small contraction/expansion movements while moving through neighboring sites. Consequently, this ends up shaping the dynamic behavior of IPR. Although all curves show this oscillating response, their quantitative results differ.

Following the mobilization step, the one-dimensional polaron (0% of anisotropy) increases its IPR to an average value of 0.54. Conversely, when $J_0^y = 0.5J_0^x$, the corresponding curve decreases to approximately 0.37. In contrast, the intermediate configuration with $J_0^y = 0.2J_0^x$ demonstrates a response that can be interpreted as a less pronounced version of the one-dimensional polaron case. Based on these observations, we can conclude that the polaron maintains its dynamic cohesion through different mechanisms depending on the ratio J_0^y/J_0^x, either by increasing or decreasing the IPR.

Fig. 4 provides visual evidence of these different relaxation mechanisms during the polaron transport. Fig. 4(a), (d), and (g) refer, respectively, to the molecular charge density at row j = 10 when J_0^y = 0.5, 0.2, and $0.0J_0^x$. For all of them, hot colors indicate a high local charge accumulation, while cold tones represent low density.

In the first heatmap (Fig. 4(a)), a distinctly localized charge accumulation is evident near the position of 9 nm, representing the polaron charge. As time progresses, the structure begins to drift under the influence of the electric field, covering a distance of 3 nm by 6 ps. It is noteworthy that immediately after the motion commences, the central region of the quasiparticle transitions from red to a yellow-based tone, indicating a decrease in charge density (ρ). This process signifies that the polaron charge has undergone delocalization, extending to at least one additional molecular unit compared to its initial localization. This observation aligns with the findings in Fig. 3(d), where a reduction in the IPR was observed after the carrier motion.

As anisotropy increases, the motion of the polaron gradually becomes more favorable, as illustrated in Fig. 4(d). In this case, when exposed to an identical electric field, the quasiparticle gains higher velocity and covers longer distances. After

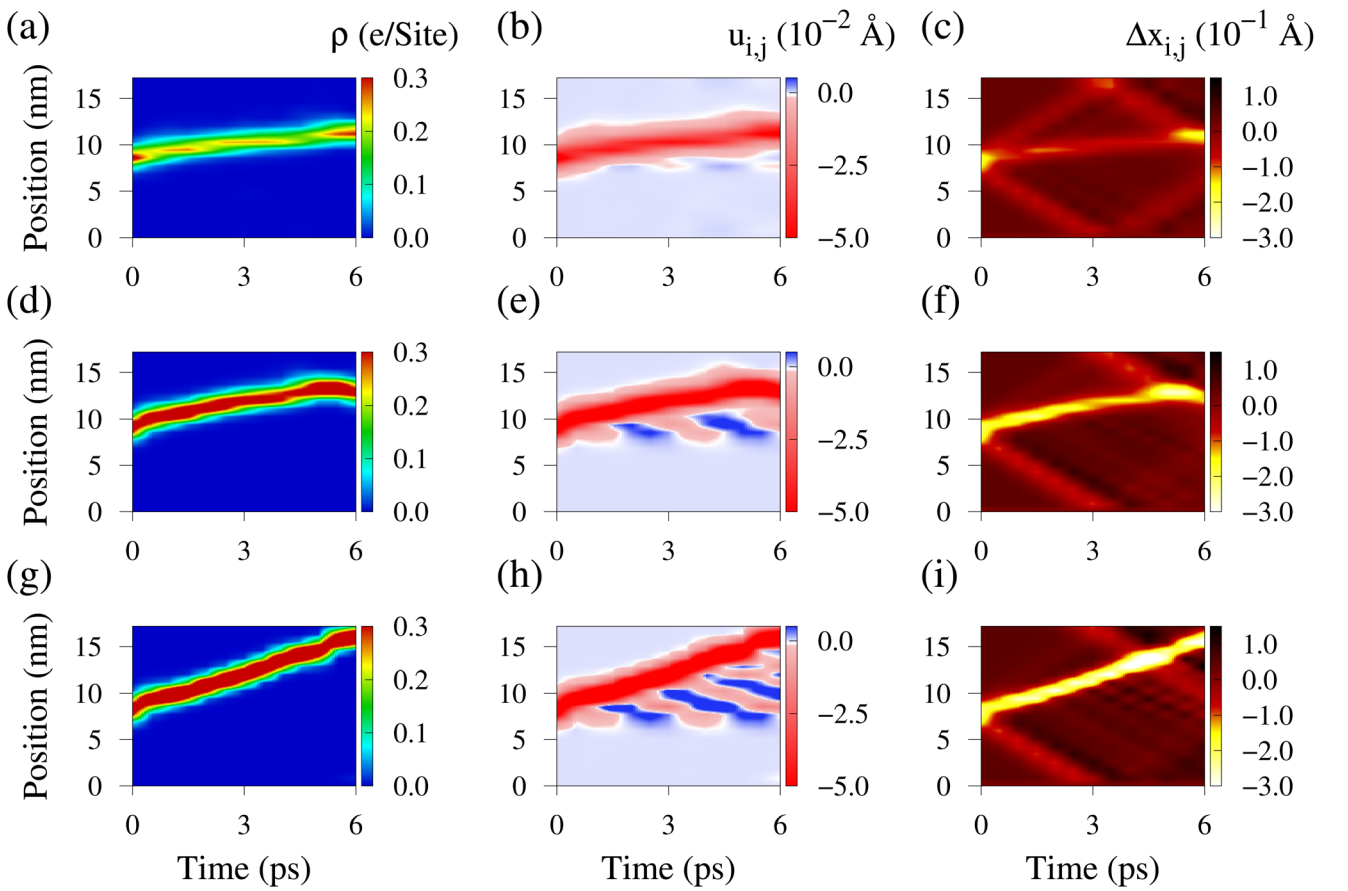

Fig. 4 The heatmap illustrates the time evolution of polaron transport in the row j = 10 under different anisotropy regimes. In panels (a), (d), and (g), the charge density profile is shown for J_0^y = 0.5, 0.2, and $0.0J_0^x$, respectively. Panels (b), (e), and (h) depict the corresponding evolution of intramolecular lattice deformation, while panels (c), (f), and (i) display the intermolecular bond length distortions.

6 ps, the carrier travels a distance of 4.8 nm, indicating a significant reduction in transport inertia. Notably, unlike the case of $J_0^y = 0.5J_0^x$, the central region of the polaron maintains a well-defined red tone throughout the entire motion, without any signs of dynamical delocalization. This behavior persists even when $J_0^y = 0$, with the only difference being that the carrier exhibits greater speed, consistent with the previous findings presented in Fig. 3.

While the charge density dynamics provide valuable insights into the polaron motion, it is important to consider that this carrier also involves phonon clouds. To capture this aspect, we present the dynamics of intramolecular lattice displacement at row $j = 10$ for different anisotropy regimes in Fig. 4(b), (e), and (h) corresponding to $J_0^y = 0.5$, 0.2, and $0.0J_0^x$. In these figures, the red regions indicate a negative value of $u_{i,j}$, *i.e.*, the internal contraction of a C_{60} molecule. Conversely, the blue regions represent its expansion, while the white areas indicate no changes in the intramolecular displacements.

In Fig. 4(b), a localized red structure can be observed, which aligns with the polaron's local charge density accumulation shown in Fig. 4(a). This deformation corresponds to the intrinsic intramolecular phonons of the quasiparticle, characterized by a series of contracted sites as seen in Fig. S2(a)–(c).† As time progresses, these contractions move collectively with the polaronic charge. By 1.5 ps, as the polaron shifts away from the sites near the 10 nm position, the region exhibits a subtle alternating blueish pattern.

The release of these fixed phonon breathers, indicated by the alternating blueish pattern, serves as a relaxation mechanism that occurs once the polaronic charge passes over those sites. In this process, the molecule retains some of the polaron's energy as an oscillating pulse. Fig. 4(e) and (h) illustrate that this mechanism becomes more pronounced in highly anisotropic configurations, leading to the appearance of more energetic phonons. This observation helps explain the tendency for ν to decrease with isotropy. As the polaron approaches a 1D quasiparticle, the relaxation process involving intramolecular phonons becomes more favorable, resulting in more sites along the molecular line containing the polaronic charge displaying non-zero values of $u_{i,j}$. Consequently, the total lattice intramolecular energy H_{intra} increases correspondingly.

To provide a comprehensive understanding of the polaron motion, we now turn to the intermolecular vibrational effects. In Fig. 4(c), (f), and (i), we observe the dynamics of the longitudinal bond length distortion $\Delta x_{i,j}$ at row $j = 10$ for different anisotropy levels: $J_0^y = 0.5$, 0.2, and $0.0J_0^x$, respectively. Regions displayed in red indicate bond expansion, while yellow tones represent contraction. Interestingly, regardless of the anisotropy level, there is a distinct pulse (propagating phonon modes) following the same trajectory as the charge density and $u_{i,j}$ heatmaps. This pulse corresponds to the polaron's intermolecular lattice deformation, wherein the collective distortion tracks the localized charge density.

The presence of the intermolecular lattice deformation signal is evident in all three configurations, but its strength increases with higher anisotropy levels. This observation aligns with the findings in Fig. S2,† where it was demonstrated that reducing dimensionality enhances the formation of more pronounced bond length distortions along the row intersecting the central region of the carrier. Notably, in Fig. 4(c), as soon as the quasiparticle initiates its motion, two identical pulses are emitted in opposite directions. This phenomenon recurs each time the polaron transitions from one site to its adjacent neighbor, albeit with decreasing magnitude, resulting in shallower phonon wave releases. These intermolecular phonons are related to the relaxation mechanism for the polaron's motion.

At around 3 ps, the most pronounced bond distortions reach a collision point due to the periodic boundary conditions. Consequently, the backward sound wave encounters the local deformation of the polaron, leading to a brief yellow signal at 6 ps in all cases. The intensity of the released phonons varies with different levels of anisotropy. In Fig. 4(f) and (i), only recoil phonons are emitted, moving in the opposite direction of the polaron's motion. These distortions exhibit greater depth compared to the case of $J_0^y = 0.5J_0^x$ (see Fig. 4(c)), and their strength increases with higher anisotropy levels.

To gain a comprehensive understanding of the system dynamics, it is necessary to evaluate the dynamical properties of all configurations within the appropriate parameter space. Fig. 5(a)–(c) present the drift velocity (V_d) heatmap as a function of the ratio between the hopping integrals and J_0^x for the field strengths $E_0 = 1$, 2 and 3 meV Å^{-1}, respectively. Hot colors indicate configurations with fast polarons, while cold colors represent slower carriers. As can be seen, the three heatmaps display qualitatively the same behavior. It can be observed that when J_0^y ranges from 0% to 30% of the x-direction hopping constant, the drift velocity (V_d) appears to be insensitive to the magnitude of J_0^x. This trend arises due to the similar effective masses of polarons under the influence of these transfer integrals.

Anisotropy, on the other hand, promotes the formation of faster carriers. The situation changes slightly when the value of J_0^y exceeds the previously mentioned threshold. In such cases, higher values of J_0^x can lead to immobile carriers, deviating from the earlier uniform response. This outcome aligns with the findings in Fig. 2 regarding polaron stability. Overall, we estimate that the carrier velocity within the $qHPC_{60}$ is approximately 0.5–1.5 nm ps^{-1}. This value is considerably lower than the velocities observed in typical OMCs (for instance, pentacene), around 2.6 nm ps^{-1}.[36] This disparity is expected since the network links in the $qHPC_{60}$ are significantly longer than the intermolecular spacing in common OMCs, and they possess relatively larger K_{inter} and α_{inter} values.

When it comes to quantitative analysis, the changes in the transport due to the field strength are significant. All the polaron velocities grow in magnitude when progressing E_0 from 1 to 3 meV Å^{-1}. This effect is especially pronounced for configurations with medium anisotropy levels (25–50%). In those cases, the velocity gain was up to 1 nm ps^{-1}. This effect is due to the energy transfer from the electric field to the polaron. The greater the field magnitude, the higher the

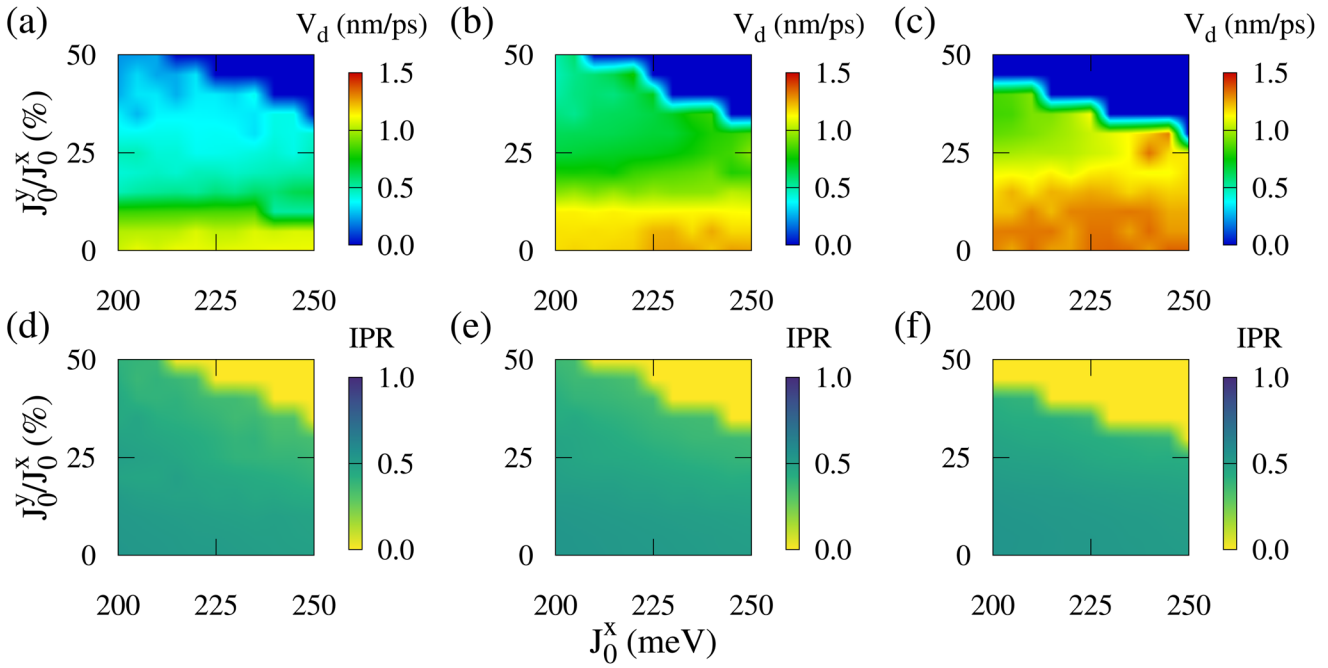

Fig. 5 Dynamical properties of polarons in $qHPC_{60}$. In panel (a)–(c), the drift velocity (V_d) heatmap is presented as function of J_0^x, and the isotropy ratio J_0^y/J_0^x for the field strengths E_0 = 1, 2 and 3 meV Å^{-1}. Hot colors refer to configurations with fast carriers, while cold tones indicate slower polarons. At panels (d)–(f), the corresponding mean IPR heatmaps are displayed.

energy given to the carrier. The result for the dynamics is a greater momentum gain for the carrier. Similar behavior is reported for OMCs[37] and other organic materials.[47,53,57,58]

It is worth mentioning that the drift velocity V_d is smaller than the bare sound velocity of the network, denoted as $V_s = a_0\sqrt{K_{inter}/M_{inter}}$.[36] In this case, V_s is equal to 2.4 nm ps^{-1}. The reason for this difference lies in the nonadiabatic nature of the polaron's drift. For the transport to occur, the carrier needs to receive energy from the electric field to overcome the potential energy barrier, enabling motion from one molecular site to another. This mechanism involves a characteristic expansion/contraction of the local charge density, which takes a transient time, effectively limiting the polaron velocity.[59]

The phonons, on the other hand, are not subject to this constraint. They transition through the lattice without delay, as their drifting does not encounter similar barriers. The only exceptions occur when these pulses collide with other deformations, which can temporarily affect their motion, a phenomenon that has been widely reported.[53,56,58,60] Furthermore, the sound velocity of the network is considerably lower than estimates for OMCs, which typically range between 4.0–8.6 nm ps^{-1}.[61] This difference is attributed to the significantly higher mass M_{inter} of the C_{60} molecules. Consequently, the resulting velocity is penalized when compared to lighter molecules.

As a final result, we present the temporal mean IPR in Fig. 5(b), using the same coloring convention as Fig. S1† but with a narrower range of [0.3–0.55] for better resolution of subtle variations between the configurations. The mean IPR is calculated based on the first 5 ps of simulation to avoid artificial contributions from pulse collisions with the polaron charge.

A closer analysis reveals a correlation between IPR and V_d. Regions with low isotropy levels exhibit high IPR values, while these values progressively decrease as the ratio J_0^y/J_0^x increases. This relationship arises because anisotropy shapes the morphology of the polaron, aligning it with the x-direction, which is also the orientation of the electric field. Consequently, transport inertia decreases, resulting in an enhanced velocity gain. Simultaneously, the preferred direction has a smoothed potential energy barrier associated with the motion, enabling the polaron to maintain its dynamical cohesion.

As expected, a yellow region is observed in the upper right corner of Fig. 5(b), indicating immobile carriers (V_d = 0). This region corresponds to the blue-colored area of the upper heatmap in Fig. 5(a). However, apart from this particular spot, the overall dynamical stability is widely observed across the entire parameter space. These results provide evidence for the robust structural cohesion of large polarons, strongly suggesting their existence in $qHPC_{60}$.

Interestingly, the dynamical properties of the carriers show little variability with respect to key parameters such as J_0^x, which reinforces the reliability of our findings. The only notable exception is the anisotropy level, which has been extensively investigated, although a specific value cannot be pinpointed.

4. Conclusion

In summary, our theoretical investigation focused on understanding the charge transport mechanism in the newly syn-

thesized fullerene network, $qHPC_{60}$. We proposed a model Holstein–Peierls Hamiltonian and explored the associated parameter space. Our results provide compelling evidence that large polarons are the predominant charge carriers in this system, demonstrating remarkable stability.

We conducted a detailed analysis of the carriers' morphology, revealing a complex interplay between electronic and lattice interactions. Notably, we found that anisotropy plays a crucial role in ensuring the carriers' stability, particularly in the presence of an external electric field. These findings shed light on the intricate mechanisms governing charge transport in $qHPC_{60}$ and contribute to a deeper understanding of its unique properties.

Anisotropy plays a crucial role in shaping the morphology of the carriers, leading to a significant reduction in transport inertia along a preferred direction. Our analysis suggests that the network exhibits a minimum anisotropy coefficient of 50%, which aligns well with the material's spatial arrangement and experimental observations.[20]

In the isotropic model $qHPC_{60}$ systems, polarons exhibit significant transport inertia. As the lattice deformations extend throughout the entire lattice in the isotropic case, the energy required to mobilize the polaron becomes substantial. In other words, the carrier possesses a high effective mass. In anisotropic $qHPC_{60}$, the polaron effective mass is reduced since charge and intermolecular lattice deformations are more localized, which favors the charge transport mechanism.

The motion of polarons in model $qHPC_{60}$ is a collective phenomenon sustained by the continuous release of intra- and intermolecular phonons. Our calculations indicate that the carrier can achieve velocities ranging from 0.5 to 1.5 nm ps^{-1}, depending on the degree of anisotropy. This study provides valuable insights into the charge transport dynamics of $qHPC_{60}$, highlighting its potential as an efficient component in optoelectronic devices.

Author contributions

T. S. A. C., M. L. P. J., G. M. S: data curation, formal analysis, methodology, and writing – original draft preparation. P. H. O. N., L. A. R. J.: conceptualization, funding acquisition, and writing – reviewing. All authors reviewed the manuscript.

Conflicts of interest

The authors declare that they have no known competing financial interests or personal relationships that could have appeared to influence the work reported in this paper.

Acknowledgements

The authors gratefully acknowledge the financial support from the Brazilian Research Councils DC, CAPES, and FAPDF. P. H. O. N., L. A. R., M. L. P. J., and G. M. S. gratefully acknowledge the financial support from FAPDF. G. M. S. and P. H. O. N. gratefully acknowledges the financial support from CNPq grants 304637/2018-1 and 306080/2022-2, respectively. P. H. O. N. acknowledges the financial support from FAP-DF grant 00193-00001831/2023-47. This work was financed by the Coordenação de Aperfeiçoamento de Pessoal de Nível Superior (CAPES) – finance code 001 and grant 88887-691997/2022-00 and Conselho Nacional de Desenvolvimento Cientifico e Tecnológico (CNPq). L. A. R. J. acknowledges the financial support from FAPDF grants 00193-00001782/2023-42, 00193-00001857/2023-95, and 00193-00001808/2022-71, FAPDF-PRONEM grant 00193.00001247/2021-20, and CNPq grant 350176/2022-1. M. L. P. J. acknowledges the financial support from FAP-DF grant $00193-00001807/2023-16$. M. L. P. J., and L. A. R. J. acknowledges Núcleo de Computação de Alto Desempenho (NACAD) and for providing the computational facilities. This work used resources of the Centro Nacional de Processamento de Alto Desempenho em São Paulo - CENAPAD-SP (proj634, and proj960).

References

1 E. Menard, M. A. Meitl, Y. Sun, J.-U. Park, D. J.-L. Shir, Y.-S. Nam, S. Jeon and J. A. Rogers, *Chem. Rev.*, 2007, **107**, 1117–1160.
2 O. Ostroverkhova, *Chem. Rev.*, 2016, **116**, 13279–13412.
3 H. Lai and F. He, *Adv. Energy Mater.*, 2020, **10**, 2002678.
4 V. Coropceanu, J. Cornil, D. A. da Silva Filho, Y. Olivier, R. Silbey and J.-L. Brédas, *Chem. Rev.*, 2007, **107**, 926–952.
5 M. Gershenson, V. Podzorov and A. Morpurgo, *Rev. Mod. Phys.*, 2006, **78**, 973.
6 C. Reese and Z. Bao, *Mater. Today*, 2007, **10**, 20–27.
7 T. He, M. Stolte, C. Burschka, N. H. Hansen, T. Musiol, D. Kälblein, J. Pflaum, X. Tao, J. Brill and F. Würthner, *Nat. Commun.*, 2015, **6**, 5954.
8 Y. An and H. Wang, *J. Mater. Sci.: Mater. Electron.*, 2023, **34**, 665.
9 Q. Di, L. Li, X. Miao, L. Lan, X. Yu, B. Liu, Y. Yi, P. Naumov and H. Zhang, *Nat. Commun.*, 2022, **13**, 5280.
10 P. Naumov, S. Chizhik, M. K. Panda, N. K. Nath and E. Boldyreva, *Chem. Rev.*, 2015, **115**, 12440–12490.
11 H. Liu, Z. Bian, Q. Cheng, L. Lan, Y. Wang and H. Zhang, *Chem. Sci.*, 2019, **10**, 227–232.
12 L. Catalano, D. P. Karothu, S. Schramm, E. Ahmed, R. Rezgui, T. J. Barber, A. Famulari and P. Naumov, *Angew. Chem., Int. Ed.*, 2018, **57**, 17254–17258.
13 X. Fan, N. Soin, H. Li, H. Li, X. Xia and J. Geng, *Energy Environ. Mater.*, 2020, **3**, 469–491.
14 C.-Z. Li, H.-L. Yip and A. K.-Y. Jen, *J. Mater. Chem.*, 2012, **22**, 4161–4177.
15 A. Pivrikas, N. S. Sariciftci, G. Juška and R. Österbacka, *Prog. Photovoltaics*, 2007, **15**, 677–696.
16 A. Ali, D. Said, M. Khayyat, M. Boustimi and R. Seoudi, *Results Phys.*, 2020, **16**, 102819.

17 D. Hu, Q. Yang, H. Chen, F. Wobben, V. M. Le Corre, R. Singh, T. Liu, R. Ma, H. Tang, L. J. A. Koster, *et al.*, *Energy Environ. Sci.*, 2020, **13**, 2134–2141.
18 T. L. Nguyen, T. H. Lee, B. Gautam, S. Y. Park, K. Gundogdu, J. Y. Kim and H. Y. Woo, *Adv. Funct. Mater.*, 2017, **27**, 1702474.
19 C. Reddy, Z. Gen Yu and Y.-W. Zhang, *Sci. Rep.*, 2015, **5**, 12221.
20 L. Hou, X. Cui, B. Guan, S. Wang, R. Li, Y. Liu, D. Zhu and J. Zheng, *Nature*, 2022, **606**, 507–510.
21 G. Shen, L. Li, S. Tang, J. Jin, X.-J. Chen and Q. Peng, *Crystals*, 2023, **13**, 224.
22 B. Mortazavi and X. Zhuang, *Coatings*, 2022, **12**, 1171.
23 R. M. Tromer, L. A. Ribeiro Junior and D. S. Galvão, *Chem. Phys. Lett.*, 2022, **804**, 139925.
24 B. Peng, *Nano Lett.*, 2023, **2**, 652–658.
25 S. Zhao, X. Zhang, Y. Ni, Q. Peng and Y. Wei, *Carbon*, 2023, **202**, 118–124.
26 L. Yu, J. Xu, B. Peng, G. Qin and G. Su, *J. Phys. Chem. Lett.*, 2022, **13**, 11622–11629.
27 W. Li, R. Yang and M. Sun, *J. Mater. Chem. A*, 2023, **11**, 3949–3960.
28 B. Peng, *J. Am. Chem. Soc.*, 2022, **144**, 19921–19931.
29 A. J. Heeger, *Angew. Chem., Int. Ed.*, 2001, **40**, 2591–2611.
30 Y. Li, V. Coropceanu and J.-L. Brédas, *J. Chem. Phys.*, 2013, **138**, 204713.
31 S. Giannini, O. G. Ziogos, A. Carof, M. Ellis and J. Blumberger, *Adv. Theory Simul.*, 2020, **3**, 2000093.
32 A. Troisi and G. Orlandi, *Phys. Rev. Lett.*, 2006, **96**, 086601.
33 F. Ortmann, F. Bechstedt and K. Hannewald, *New J. Phys.*, 2010, **12**, 023011.
34 L. Song and Q. Shi, *J. Chem. Phys.*, 2015, **142**, 174103.
35 L. Wang, O. V. Prezhdo and D. Beljonne, *Phys. Chem. Chem. Phys.*, 2015, **17**, 12395–12406.
36 E. Mozafari and S. Stafström, *J. Chem. Phys.*, 2013, **138**, 184104.
37 M. L. Pereira Jr., W. F. da Cunha, R. T. de Sousa Jr., G. M. e Silva and L. A. Ribeiro Jr., *J. Phys. Chem. C*, 2019, **123**, 13410–13418.
38 Z. Shuai, L. Wang and Q. Li, *Adv. Mater.*, 2011, **23**, 1145–1153.
39 J. H. Fetherolf, D. Golež and T. C. Berkelbach, *Phys. Rev. X*, 2020, **10**, 021062.
40 M. L. Pereira Jr., R. T. de Sousa Jr., G. M. e Silva and L. A. Ribeiro Jr., *J. Phys. Chem. C*, 2019, **123**, 4715–4720.
41 S. Margadonna and K. Prassides, *J. Solid State Chem.*, 2002, **168**, 639–652.
42 S. Stafström, *Chem. Soc. Rev.*, 2010, **39**, 2484–2499.
43 E. Mozafari and S. Stafström, *Phys. Lett. A*, 2012, **376**, 1807–1811.
44 L. A. Ribeiro and S. Stafström, *Phys. Chem. Chem. Phys.*, 2016, **18**, 1386–1391.
45 Y. Ono and A. Terai, *J. Phys. Soc. Jpn.*, 1990, **59**, 2893–2904.
46 G. M. e Silva, *Phys. Rev. B: Condens. Matter Mater. Phys.*, 2000, **61**, 10777.
47 T. d. S. A. Cassiano, L. E. de Sousa, L. A. Ribeiro Junior, G. M. e Silva and P. H. de Oliveira Neto, *Synth. Met.*, 2022, **287**, 117056.
48 M. Riedmiller and H. Braun, IEEE international conference on neural networks, 1993, pp. 586–591.
49 M. L. Pereira Junior, R. T. de Sousa Júnior, G. M. e Silva and L. A. Ribeiro Junior, *Phys. Chem. Chem. Phys.*, 2019, **21**, 2727–2733.
50 L. A. R. Junior and S. Stafström, *Phys. Chem. Chem. Phys.*, 2017, **19**, 4078–4084.
51 W. Krätschmer, L. D. Lamb, K. Fostiropoulos and D. R. Huffman, *Nature*, 1990, **347**, 354–358.
52 K. Yabana and G. Bertsch, *Phys. Scr.*, 1993, **48**, 633.
53 A. A. Johansson and S. Stafström, *Phys. Rev. B: Condens. Matter Mater. Phys.*, 2004, **69**, 235205.
54 T. Astakhova and G. Vinogradov, *Eur. Phys. J. B*, 2019, **92**, 1–9.
55 H. Wang, H.-Y. Shi, X.-J. Yuan, J.-F. Zhao, H.-X. Bu and G.-C. Hu, *J. Phys. Chem. Lett.*, 2022, **13**, 614–621.
56 T. d. S. A. Cassiano, P. H. de Oliveira Neto and G. M. e Silva, *Sci. Rep.*, 2022, **12**, 7967.
57 Å. Johansson and S. Stafström, *Phys. Rev. Lett.*, 2001, **86**, 3602.
58 M. B. Falleiros and G. M. e Silva, *J. Phys. Chem. A*, 2019, **123**, 1319–1327.
59 L. A. R. Junior and S. Stafström, *Phys. Chem. Chem. Phys.*, 2015, **17**, 8973–8982.
60 W. F. da Cunha, P. H. de Oliveira Neto, A. Terai and G. M. e Silva, *Phys. Rev. B*, 2016, **94**, 014301.
61 M. L. Pereira Junior and L. A. Ribeiro Junior, *J. Mol. Model.*, 2017, **23**, 1–7.

